Antimicrobial peptide mechanism revealed with scattering-guided molecular dynamics simulation

Robert Allsopp[1], *Anna Pavlova*[2], *Tyler Cline*[1], *Aria M. Salyapongse*[3], *Richard E. Gillilan*[4], *Y. Peter Di*[5], *Berthony Deslouches*[5], *Jeffery B. Klauda*[1*], *James C. Gumbart*[2*], *Stephanie Tristram-Nagle*[3**]

[1]Department of Chemical and Biomolecular Engineering, University of Maryland, College Park, MD 20742

[2]School of Physics, Georgia Institute of Technology, Atlanta, GA, 30332

[3]Biological Physics Group, Physics Department, Carnegie Mellon University, Pittsburgh, PA, 15213

[4]Cornell High Energy Synchrotron Source (CHESS), Cornell University, Ithaca, NY, 14853

[5]Department of Environmental and Occupational Health, University of Pittsburgh, Pittsburgh, PA, 15260

***Corresponding author, stn@cmu.edu, Stephanie Tristram-Nagle,* Biological Physics Group, Physics Department, Carnegie Mellon University, 5000 Forbes Avenue, Pittsburgh, PA 15213, https://www.cmu.edu/biolphys/jfstn 412-268-3174 (work), 412-680-8640 (mobile), 412-681-0648 (FAX)

**Co-corresponding author, jbklauda@umd.edu, Jeffery B. Klauda,* Department of Chemical and Biomolecular Engineering, 2113 Building 90, University of Maryland, College Park, MD 20742, https://user.eng.umd.edu/~jbklauda/index.html, 301-314-9126 (work), 732-910-3244 (mobile), 301-314-9126 (FAX)

**Co-corresponding author, gumbart@physics.gatech.edu James C. Gumbart,* School of Physics, 837 State St NW, Georgia Institute of Technology, Atlanta, GA, 30332, https://simbac.gatech.edu, 404-385-0797 (work), 309-255-9869 (mobile), 404-894-9958 (FAX)

Keywords: x-ray diffuse scattering, neutron reflectometry, molecular dynamics simulations, antimicrobial peptides, lipid model membranes (LMMs), Gram-negative bacteria, Gram-positive bacteria

Abstract. In an effort to combat rising antimicrobial resistance, our labs have rationally designed cationic, helical amphipathic antimicrobial peptides (AMPs) as alternatives to traditional antibiotics, since AMPs incur bacterial resistance in weeks, rather than days. One highly positively charged AMP, WLBU2 (+13 e), (**RR**WV **RR**V**R R**WV**R R**VV**R** VV**RR** WV**RR**), has been shown to be effective in killing both Gram-negative (G(-)) and Gram-positive (G(+)) bacteria by directly perturbing the bacterial membrane non-specifically. Previously, we used two equilibrium experimental methods: Synchrotron x-ray diffuse scattering (XDS) providing lipid membrane thickness, and neutron reflectometry (NR) providing WLBU2 depth of penetration into three lipid model membranes (LMMs). The purpose of the present study is to use molecular dynamics (MD) simulations to investigate the detailed biophysics of the interactions of WLBU2 with lipid membrane mimics of Gram-negative outer and inner membranes, and Gram-positive cell membranes, to determine the mechanisms of bacterial killing. Instead of coarse-graining, backmapping or simulating without bias for several microseconds, all-atom (AA) simulations were guided by the experimental results and then equilibrated for ~0.5μs. Multiple replicas of the inserted peptide were run to probe stability and reach a combined time of at least 1.2 μs for G(-) and also 2.0 μs for G(+). In addition, there were additional preliminary trials that were used to determine the best surface tension conditions to run at so, but the exact time is unknown. The simulations with experimental comparisons help rule out certain structures and orientations, and propose the most likely set of structures, orientations and effect on the membrane. The simulations revealed that water enters into the hydrocarbon core when WLBU2 is positioned there. For an inserted peptide, the three types of amino acids (R,W,V) are arranged with W and V more centrally located, and the 13 R's extending from the core to the interface. For a surface state, R, W and V are positioned relative to the bilayer interface as expected, with R closest to the water interface.

Abbreviations. AA, all-atom; APL, area per lipid; ATR-FTIR, attenuated total reflection-Fourier transform infrared spectroscopy; AMP, antimicrobial peptide; CHESS (Cornell High Energy Synchrotron Source); CD, circular dichroism; CPP, cell-penetrating peptide; DLPG, 1,2-dilauroyl-*sn*-glycero-3-phospho-(1'-rac-glycerol); DOTAP, 1,2-dioleoyl-3-trimethylammonium-propane (chloride salt); EDP, electron density profile; G(-), Gram-negative; G(+), Gram-positive; HIP, hexafluoroisopropanol; IM, inner membrane; K^+, potassium ions; KDO2, 3-deoxy-D-manno-octulosonic acid; lipid model membranes (LMMs); LPS, lipopolysaccharide; Na^+, sodium ions; NMR, nuclear magnetic resonance; NR, neutron reflectivity; OM, outer membrane; PBS, phosphate buffered saline; POPE, 1-palmitoy-2-oleoyl-*sn*-glycero-3-phosphoethanolamine; POPG, 1-palmitoyl-2-oleoyl-*sn*-glycero-3- phospho-(10-rac-glycerol) sodium salt; R, arginine; SAXS, small angle x-ray scattering; SFG, sum frequency generation; TOCL, 10,30-bis-[1,2-dioleoyl-sn-glycero-3-phospho]-*sn*-glycerol sodium salt; V, valine; W, tryptophan; XDS, x-ray diffuse scattering

Introduction

While traditional antibiotics have long provided protection against bacterial infection and have allowed surgical interventions to save lives, the world-wide problem of bacterial resistance[1] continues to motivate many researchers to explore alternatives. A comprehensive report aimed at assessing rising antimicrobial resistance has predicted that by 2050, over 10 million deaths will occur annually as a result of antimicrobial resistant pathogens[2]. One approach to solving this problem is to use rational design to synthesize antimicrobial peptides (AMPs) as an alternative antibiotic because of the delay in resistance. The Montelaro/Deslouches groups were inspired by the human cathelicidin, LL-37, a helical, broad-spectrum amphipathic peptide of 37 amino acids with 12 positively charged residues[3, 4]. A second inspiration was the naturally-occurring AMP on the extreme end of the C-terminal tail of the HIV-1 fusion protein, LLP1, which is also highly cationic, containing 7 positively charged residues out of 28 residues[5]. The highly cationic nature of these peptides is thought to impart selectivity towards negatively charged bacterial cells, and lower their toxicity to eukaryotic cells[6]. The Deslouches lab has attempted to discover key aspects of AMP-caused bacterial killing by synthesizing simplified AMPs containing only 3 types of amino acids: valine (V), tryptophan (W) and arginine (R)[4, 7-10], instead of 15 types as in LL-37 or 11 types as in LLP1. By limiting the number of types of amino acids, we can determine precisely which physical properties, hydrophobicity, hydrophobic moment, length and charge of peptides, are essential for activity. For the present work, we have focused on the rationally designed, cationic AMP WLBU2[11-13], which is now in Phase II clinical trials for wound healing[14].

The primary structure of WLBU2 is **RR**WV **RRV**R **R**WV**R** R**V**V**R** VV**RR** WV**RR,** with 13 R residues (shown in bold type) out of 24 amino acid residues. If WLBU2 were perfectly α-helical, the helical wheel design would predict that the R's line the hydrophilic face while the V's line the hydrophobic face toward the lipid chains, with the W's close to the interface between these two faces (Figure 1). W was

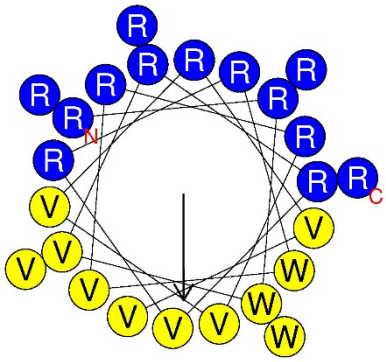

Figure 1. Helical wheel diagram of WLBU2 prepared using the Heliquest WEBsite (heliquest.ipmc.cnrs.fr). Arrow shows the direction of the hydrophobic moment, μH.

added since it stabilizes the AMP in saline conditions, such as in the human body[13]. The detailed secondary structure of WLBU2 in four different lipid model membranes (LMMs) and in aqueous solution was obtained using circular dichroism spectroscopy and was published previously[15]. While WLBU2 in water or 15 mM phosphate buffered saline (PBS) adopts primarily a random coil or β-sheet structure, the α helical content increases to ~75% in Gram-negative (G(-)) inner membrane (IM) or Gram-positive (G(+)) LMMs, and to ~40% in lipopolysaccharide (LPS)-containing LMMs.

Although WLBU2 is not 100% helical by our determination, it is still primarily helical when in contact with the inner membrane of G(-) and G(+) LMMs, partially confirming the locations of R and V on opposite faces in WLBU2's helical wheel rational design. In a eukaryotic membrane mimic, we found only a low level of α-helicity (~20%)[15]. Thus, the secondary structure of WLBU2 plays an important role in its ability to avoid toxicity to eukaryotic cells.

For the current study, we implement molecular dynamics (MD) simulations to visualize orientations of WLBU2 when interacting with four different bacterial LMMs. By constraining the thickness of the different LMMs to those obtained using x-ray diffuse scattering (XDS), and the locations of the peptide to those obtained using neutron reflectometry (NR), a starting point for the simulation is obtained. Then, by simulating for an additional ~400 nanoseconds, the conformation of WLBU2 and the surrounding lipids are allowed to equilibrate to the final membrane-peptide structure and an electron density profile (EDP) is produced. Fourier transformation of the EDP produces a continuous form factor ($F(q_z)$). By comparing the simulated $F(q_z)$ with the experimental $F(q_z)$ obtained using x-ray diffuse scattering (XDS), the simulation's accuracy is determined. This comparison anchors the all-atom (AA) MD simulation to the experimentally determined lipid thickness and structure, which sometimes requires applying a surface tension in the simulation. We show simulation/experimental comparisons for four LMMs that mimic the outer (LPS and KDO2) and inner G(-) membranes and the G(+) cell membrane. The LMMs are constructed of mixtures of pure lipids that mimic the lipid composition of bacterial cells[16]. Molecular details of WLBU2's conformation in the membrane give insights into the mechanism of bacterial killing by WLBU2's membrane perturbation.

Materials and methods

MD simulations

KDO2. The KDO2 simulations were previously published in Ref. [15]. For convenience, these methods and results are found in the S.I. and in Fig. S1.

G(-) membrane inner membrane (IM). Each simulation involved membranes with lipids that were composed of POPE/POPG/TOCL in a 7:2:1 molar ratio, as in the scattering experiments. Each simulation had either one or two peptides that were placed in different locations, with either 100 or 160 total lipids. The simulations were created using 45-60 TIPS3P waters per lipid[17] and 27-38 K^+ ions depending on the size of the simulation. Simulations were run on the Extreme Science and Engineering Discovery Environment (XSEDE) using the Texas Advanced Computing Cluster (TACC) on Stampede2, and also on Comet and Expanse at the San Diego Super-computer Center at U.C. San Diego. The simulations were run for 300 ns for the surface simulations, and at least 420 ns for the inserted simulations to ensure stability. It was known from the beginning that the peptide easily comes out of the membrane and that it was a challenge to sustain the peptide inside the membrane. This only became possible when the surface tension was adjusted to make room for the lipids to sink deeper into the membrane and agree better with the experimental data. The simulations of the straight peptide inserted into the membrane were considered but proved unstable. Later it was determined that such an orientation would more likely span straight through the membrane yielding a constant density across the membrane. However, that does not agree as well with the neutron density showing variability within the membrane, so it would have to favor one side over the other, and that is seen in our bent inserted structure. Additional details concerning the stability of the inserted peptide position are given in S.I. (see Figs. S2 and S3).

The peptide was never restrained for the G(-) trials. The only bias was the use of additional surface tension that was later adjusted and reduced to finally optimize the fit by taking the last 100ns for analysis. The initial location and number of peptides were varied, as was the surface tension (from 0 to 15 mN/m). All surface simulations were run with NPT or NPγT. The calculated form factors were used as a measure of success for the different simulations, focusing on the cross-over points (zero positions) on the x-axis and lobe relative peak heights, and their comparison to XDS experiment.

The need for adding additional surface tension ~9 dyne/cm likely arose from small inaccuracies in the force field (lipid-lipid and protein-lipid interactions). To reduce the system size, unwanted interactions, and complexity, the peptides were simulated separately in two states (surface-bound and inserted). The surface tension applied for the surface-bound and inserted states of WLBU2 varied because the initial optimization of the inserted peptide revealed huge errors in certain regions of low q-space when the surface tension was the same as the surface-bound state. There are several surface tension combinations that would match the

form factor crossing points, but from experience the best combination to lower the sum squared error was the 9 dyne/cm for the surface bound and the 15 dyne/cm for the inserted WLBU2. Other combinations fit the crossing points but they did not provide the optimal lobe heights. Additionally, the surface bound peptides had a surface tension that matched the surface tension of the control G(-) membrane indicating that the surface configuration did not contribute any to the surface tension of the system. Instead, the small shift that is observed is caused entirely by the inserted peptides. This was the best way to optimize the crossing points and the peak heights while interpreting the NR data.

MD simulations of G(-) membranes utilized NAMD 2.12-2.14 depending on the resource[18], while also using the CHARMM36 force field for lipids[19] and CHARMM36m force field for proteins[20]. A 2-fs time step was employed with long- range electrostatics interactions evaluated every other time step using the particle mesh Ewald method[21]. Short-range non-bonded interactions were cut off at 12 Å using a force-based switching function beginning at 10 Å. Temperature was maintained at 37 $^{\circ}$C using Langevin dynamics, and pressure was maintained separately in the membrane-planar (when no surface tension was applied) and membrane-orthogonal direction using a Langevin piston at 1 atm.

G(+) membrane. The G(+) membrane model was comprised of POPG/POPE/DOTAP/TOCL in a 6:1.5:1.5:1 molar ratio, which has one protonated phosphate group and charge -1e, equally distributed between the two leaflets, for a total of 80 lipids. A total of 5665 TIP3P water molecules and 44 Na+ ions were added. The system was run for 300 ns. The system was also run for 300 ns under an applied surface tension of 9 mN/m. The simulations were carried out at 37 $^{\circ}$C.

The WLBU2 peptide was added to the surface of the G(+) membrane in the straight and bent conformations. Each system was run for 400 ns under an applied surface tension of 9 mN/m; the last 100 ns were used for analysis. For comparison, an additional simulation of an alternative bent surface conformation was run for 400 ns equilibration and 400 ns with 9 dyne/cm applied. A model with the peptide inserted in the center of the membrane was also simulated. In order to stabilize the WLBU2 peptide at the center of the membrane, Tcl boundary forces in NAMD were used to create space by slowly pushing the lipids outward over the course of ~20 ns. Once there was enough space for the peptide, it was inserted and then held fixed for 150 ns while lipids equilibrated around it. Water was also prevented from going into the membrane during this process. The inserted model was then run under no surface tension for 100 ns, followed by 15 dyne/cm surface tension for 200 ns with the peptide restrained, and then 200 ns with no peptide restraint. All simulation parameters were the same as those used for the G(-) membrane, although NAMD 3 on GPUs was used for some runs [18]. Additional details concerning the stability of the inserted peptide position are given in S.I. (see Fig. S4).

LPS membrane. The symmetric pure LPS membrane was a mixture of 24 *P. aeruginosa* Type 1 (six acyl chains) and 48 Type 2 (five acyl chains) LPS equally distributed between the

two leaflets. The lipid/peptide molar ratio was 72:1, close to the XDS lipid/peptide molar ratio of 75:1. Each LPS molecule was capped with ten core 1b sugars and had a charge of -10e. The membrane was built using CHARMM-GUI [22, 23], and was solvated above and below with 15269 total TIP3P water molecules and 720 Na+ ions to neutralize the system. Because the phosphate group on LPS may be protonated [24], we modeled both the fully deprotonated (-10e) and singly protonated on each phosphate (-8e) LPS, with the latter having a corresponding reduction in Na+ ions. The systems were equilibrated for 200 ns with the last 100 ns used for analysis. The other simulation details are the same as for G(+) membrane, including the system with WLBU2 in the center of the membrane.

Electron density profiles (EDPs) from simulation. Simulated form factors were produced from the SIM file which identifies all atoms and their positions in the bilayer, using the SimtoExp software[25]. EDPs, which are the Fourier transform of the form factors, were also produced using the SimtoExp software. The SimtoExp software finds a chi-square goodness of fit between the experimental and simulated form factors.

Robetta modeling. An initial protein starting structure is required for simulations. For this, the Robetta[26, 27] server was utilized. Robetta is an online protein prediction server developed by the Baker Laboratory at the University of Washington. Robetta uses the Ginzu prediction protocol to match protein chains into putative domains with reasonable confidence. The structure and 3-D models are constructed using homology modeling with comparisons made to proteins with solved structures, and *ab initio* structure prediction methods designed by the Robetta server. A shortcoming of Robetta is that its *de novo* modeling stems from the assumption that proteins typically form a soluble domain with a hydrophobic core, whereas short sequences such as the 24-mer WLBU2 often do not follow this trend. As a result, the Robetta server has a 28-residue minimum input length, so two valine residues were added to the C-terminus and N-terminus each of WLBU2. Valine was chosen as the additive to reduce steric and electrostatic effects. After Robetta outputted the potential initial structure, the four added valine residues were spliced out to recover the original 24-residues WLBU2. Robetta returned with confidence two distinct models for WLBU2. Since both models (see Fig. 2(a),(b)) were predicted with confidence using the Robetta server, both were considered potential starting structures for the simulations in this work. However, the bent helix conformed better to the secondary structure obtained using circular dichroism (CD)[15].

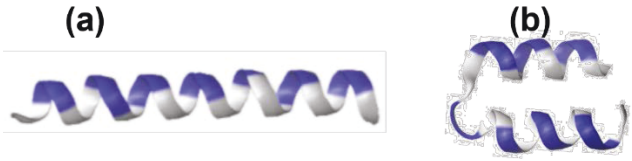

Figure 2. Structural predictions from the Robetta software. (a) Straight helix. (b) Bent helix. Colors: R, blue; W, V, white.

X-ray diffuse scattering (XDS) and neutron reflectivity (NR) materials and methods. No new NR data were obtained for the present work; the NR materials and methods and results were previously published in SI in Ref.[15] and are reproduced in S.I. for convenience. While most of the XDS data were previously published in [15], additional XDS were obtained of the G(-) control for the purpose of judging the reproducibility of the experimental form factors. For this comparison, G(-) control data were obtained on two virtual CHESS trips and compared to CHESS data collected in 2018, where sample substrate was varied as was the method of data collection. In 2018, samples were deposited onto flat silicon wafers which were rotated in order to x-ray all of the angles equally, using a motorized internal rotation within the hydration chamber. In November, 2020, samples were deposited onto highly polished, cut quartz glass rods of radius 9 mm that were not rotated in the beam. In June, 2021, samples were deposited onto flat silicon wafers which were rotated using a large rotation motor, external to the chamber. The XDS methods from Ref. [15] are reproduced in S.I. for convenience. A previously unpublished image of XDS for G(-) control is shown as an example of x-ray diffuse scattering in Fig. 3.

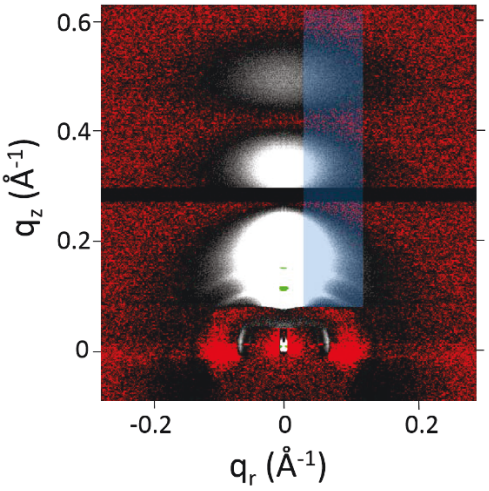

Figure 3. G(-) IM control. 2D image collected at CHESS at 37 °C using the Eiger 4M hybrid detector in November, 2020. Sample was oriented onto a cut, quartz glass rod. Intensity in white lobes underneath blue swath provides the intensity data for the form factor data to compare to MD simulation. Green spots correspond to lamellar orders, n = 3 and 4. Black horizontal line at q_z ≈ 0.3 Å^{-1} is due to the separation between panels in the detector.

Results

Neutron reflectivity (NR)

NR informs about the location of WLBU2 in the membrane. This is a key metric for the accuracy of the MD simulations since it constrains them to consider an internal location in the hydrocarbon region. Since this AMP, WLBU2, is highly cationic (+13), it is not intuitive that it would locate in the hydrocarbon region. Nevertheless, the NR shows two possible locations for WLBU2, in the headgroup and in the hydrocarbon region (Fig. S5). The dual location is the case for both G(-) inner membrane (Fig. S5(b)) and G(+) (Fig. S5(c)) membrane mimics. For KDO2 the data in Fig. S5(a) show that WLBU2 locates only in the headgroup region, whereas for LPS,

WLBU2 is located only in the hydrocarbon region in Fig. S5(d). Fig. S5 was previously published in Ref.[15] and is reproduced in S.M. with permission since it is relevant for the present work. The MD simulations in the present work used these peptide locations in different membrane mimics.

XDS – form factors

As described in S.I. and shown in Fig. S6, the XDS intensity gets converted into a form factor, which is the first step in comparing to the form factor obtained from MD simulation. The sharp minima in Fig. S6, at $|F(q_z)| = 0$ e/Å^2 are related to the thickness of the membrane. If these minima move in q_z (Å^{-1}) to larger values, this indicates that the membrane thins. Thus, we can compare directly the form-factors from the MD simulation with the experimental form factors, to ascertain if the membrane thickness is the same. We investigated the reproducibility of these minima (also known as cross-over, or zero points), at $q_z \approx 0.26$ Å^{-1} and $q_z \approx 0.40$ Å^{-1} by making many scans of G(-) IM control on two different substrates (silicon wafers and cut glass rods). As shown in Fig. 4 there is little variability in the cross-over points between different samples. This indicates that in spite of three different sample-to-detector distances and three different wavelengths, when converted pixels to q_z values, there is very good agreement. There is some variability in the ratio of amplitudes which is attributed to inhomogeneities in the sample thickness. This inhomogeneity was more apparent in the samples prepared on cut glass rods where the Rock and Roll procedure is problematic due to the cylindrical geometry. Cut glass rods were used in one virtual run at CHESS, in place of rotating a flat sample from -1.6 to 7 degrees during the data collection.

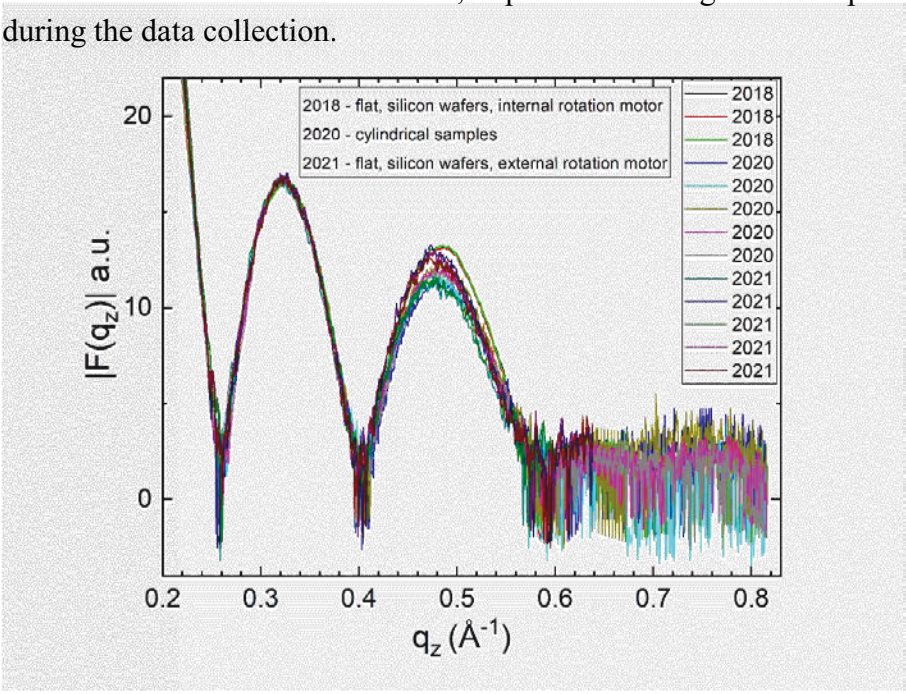

Figure 4. Form factor data for G(-) IM LMMl control obtained at CHESS at 37 °C on cut glass rods or on flat, highly polished silicon wafers that were rotated either externally or internally during data collection (see legend). Amplitudes were normalized in the first, full lobe. G(-) LMM: POPE:POPG:TOCL (7:2:1 molar ratio).

Comparison of experimental and simulated form factors

KDO2

Fig. S1 shows the MD simulation and experimental results for KDO2. This figure was previously published in Ref.[15], but is included in this work in the S.I. for convenient comparison to the other three new MD simulations. In Fig. S1(a), the form factor that results from the MD simulation is directly compared to that from the XDS experiment for pure KDO2. For this comparison we used the MD simulation with doubly deprotonated phosphate groups, with a net negative charge of -6 for KDO2 and 432 Na^+ ions (6/lipid). As shown there is remarkable agreement between the experimental and simulated form factors, especially the positions of the cross-over points, verifying that the force field and sampling used in the simulation accurately reproduce the equilibrium membrane structure, and that no surface tension is required. Excluding Na^+ ions in this comparison, which are present in the simulations, greatly improved the agreement with experiment. The reason for this could be because the counterion used in the XDS experiment was the ammonium ion, not sodium, which has a lower electron density and so does not contribute to XDS form factors, or that the counterion diffuses away from the lipid in the hydrated sample. Fig. S1(b) shows the EDP produced from the simulation results using the SimtoExp computer program, with component groups as in the caption. As shown, there is a double headgroup peak, due to the electron density of the two octulosonic acid residues exterior to the phosphate/mannose groups. Fig. S1(c) shows a visualization of the KDO2 simulation, prepared using Visual Molecular Dynamics (VMD)[28]. Fig. S1(d) shows the comparison of form factors for the case where WLBU2 was added to KDO2 (76:1 lipid/peptide molar ratio). In this case the singly deprotonated phosphate groups were used, giving a net negative charge of -4 to KDO2. Again, there is strikingly good agreement, showing that the protonation method did not affect these comparisons. In Fig. S1(e), the EDP shows the location of WLBU2 in the outer headgroup region of KDO2, outside of the octulosonic acid residues. This is shown visually in Fig. S1(f), where WLBU2 was initially constrained as a bent α-helix, since our circular dichroism results found it to be primarily helical, but not 100% helical, in KDO2[15]. When all constraints were removed, WLBU2 remained primarily helical. See Materials and Methods for the rationale for using a bent or a straight WLBU2.

G(-) Inner Membrane (IM)

Initial efforts to simulate the control G(-) IM model membrane were carried out without a surface tension applied, as with KDO2 (Fig. S1). Three replicas of an all-atom membrane were constructed using CHARMM-GUI's Membrane Builder[19, 23, 29, 30]. The results of this simulation of control G(-) IM are shown in Fig. 5. In Fig. 5(a), agreement between the simulated form factor (black) and experimental form factor (red) is lacking. While the amplitudes of the lobes match fairly closely, places where the $F(q_z)$ go to zero (the cross-over points) are not in good agreement. This comparison indicates that the simulated bilayer is thicker than that of the

experimental data. Fig. 5(b) shows the simulated EDP and Fig. 5(c) shows the VMD visualization.

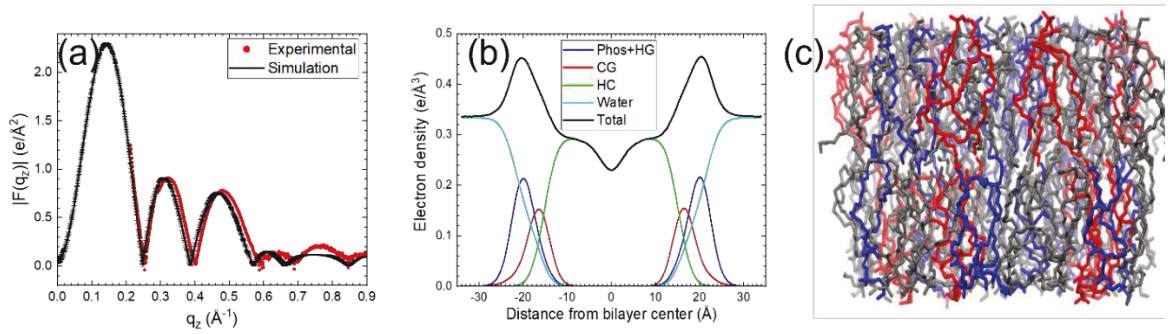

Figure 5. (a) Unsuccessful attempt to match the form factor for G(-) IM simulated without surface tension (black line) and experimental form factor (red circles). The simulated form factor data are shown as an average of 3 simulations, with standard deviations. (b) Simulated EDP. Colors: Total, black; phosphate + outer headgroup, blue; carbonyl-glycerol, red; hydrocarbon, green; water, cyan. (c) VMD visualization of simulated G(-) IM bilayer. Colors: POPE, gray; POPG, blue; TOCL, red.

In an attempt to match more closely to the experimental bilayer thickness, various small surface tensions were applied and simulated between 9 and 15 dynes/cm. This resulted in shifting the positions of the zeroes (cross-over points). The best agreement with the experimental form factor for the control G(-) EDP was observed when a surface tension of 9 dyne/cm was applied (Fig. 6(a)). Fig. 6(b) shows the simulated EDP and Fig. 6(c) shows the VMD visualization of control G(-) IM. The inclusion of potassium ions caused no change to the goodness of fit to the experimental data due to the ~15 times smaller amount compared to the sodium ions in KDO2.

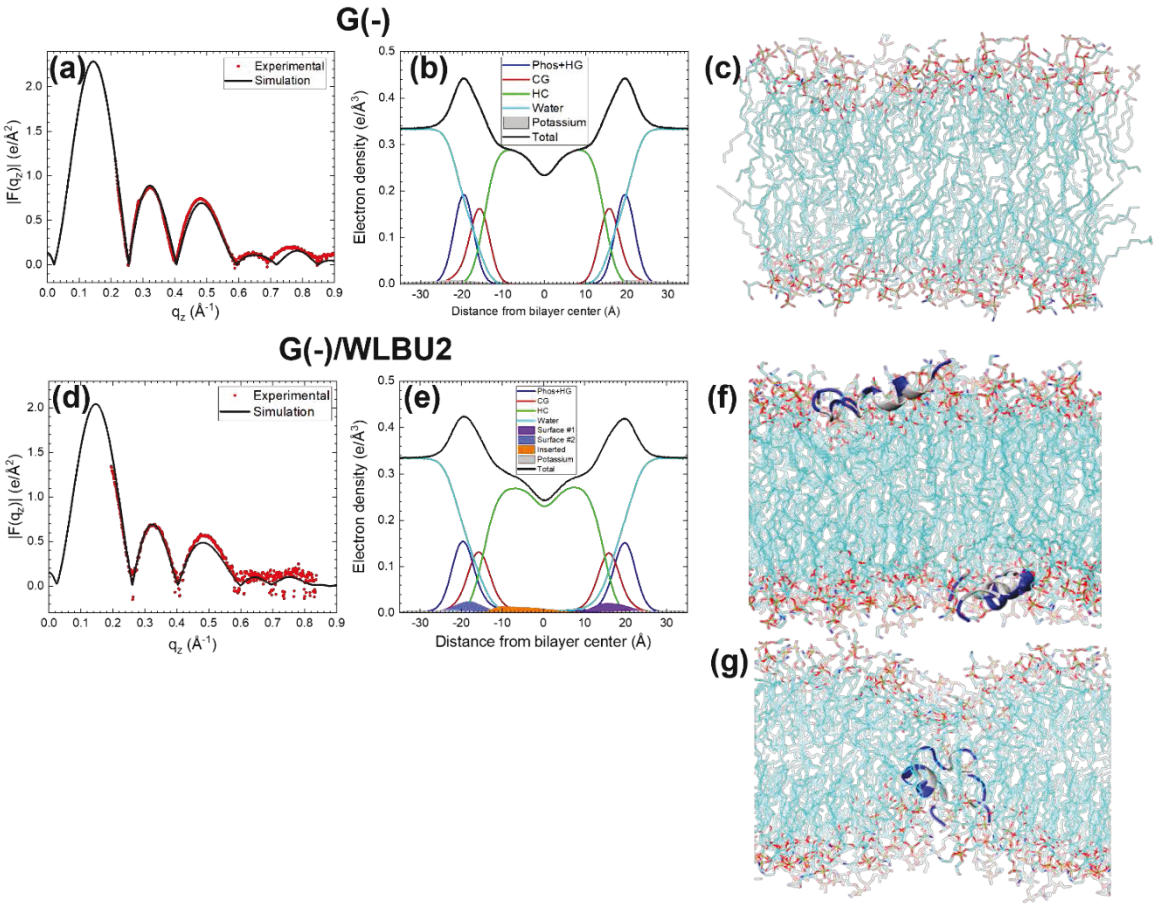

Figure 6. (a) G(-) IM control simulated (black line) and experimental form factors (red circles). (b) G(-) IM simulated EDP. Colors: Total, black; phosphate + outer headgroup, blue; carbonyl-glycerol, red; hydrocarbon, green; water, cyan; K^+, gray. (c) VMD visualization of G(-) IM control. Colors: Oxygen atoms, red; hydrocarbon chains, cyan. (d) G(-)/WLBU2 76:1, simulated (black line) and experimental form factors (red circles) (e) G(-)/WLBU2 76:1 simulated EDP. Colors: as in 6(b); surface WLBU2#1, filled purple; surface WLBU2#2, filled blue; inserted WLBU2, filled orange. (f) VMD visualization of two surface states. Colors as in 6(c); WLBU2, R, blue; W,V, white. (g) VMD visualization of inserted WLBU2. Colors as in 6(f).

Table 1. The sum of squares error (SSE) for different G(-) IM/WLBU2 simulations at 37 °C.

	1st Lobe	2nd Lobe	3rd Lobe	Total SSE (lobes + zeroes)
Combined* (shown in Fig 6(d,e))	0.53	0.16	1.00	3.07
Bent inserted 0 dyne/cm	1.36	6.71	10.04	19.72
Bent inserted 15 dyne/cm	1.04	1.74	1.60	5.66
Bent surface 0 dyne/cm	0.74	1.75	2.52	6.70
Bent surface 9 dyne/cm	0.37	0.18	1.13	3.13
Straight surface 0 dyne/cm	0.66	1.32	1.38	4.86
Straight surface 9 dyne/cm	0.39	0.20	1.34	3.52

The amplitudes of the three lobes in the experimental form factor were compared to the amplitudes of the simulated form factors. SSE of each lobe was computed along with the total SSE of the entire curve as described in Materials and Methods. *Surface tension of the combined model: 15 dyne/cm for the bent inserted WLBU2 and 9 dyne/cm for the bent surface WLBU2. The above simulation was carried out at G(-)/WLBU2 molar ratio of 87:1; a second simulation at a molar ratio of 80:1 produced similar errors.

When WLBU2 was added to the G(-) membrane mimic, the best agreement with experiment was obtained when the peptide simulated density was split into both a bent surface model at 9 dyne/cm and a bent inserted model at 15 dyne/cm (see Table 1). The weighting of the surface and inserted models was constrained to 37.2% inserted and 62.8% surface based on fitting the NR result to two Gaussians (Fig. 54(b)). Note that significant oxygen atoms from the glycerol-carbonyl, phosphate headgroups and water enter into the bilayer interior in Fig. 6(g). Table 1 shows the Sum of Squares Errors for different WLBU2 locations and surface tensions. Note that this procedure of dividing the peptide density into surface and inserted assumes that there is no interaction between the surface and inserted states of WLBU2, as we have previously performed in the case of the lung surfactant proteins SP-B and SP-C[31].

A visualization of a close-up of WLBU2 in the inserted state is shown in Fig. 7(a). When the R's are located in the center of the hydrocarbon region, K^+ ions and water are drawn into the membrane. Fig. 7(b) shows that there is significant electron density of water in the center of the bilayer in the case of inserted WLBU2, but not for the two surface states of WLBU2.

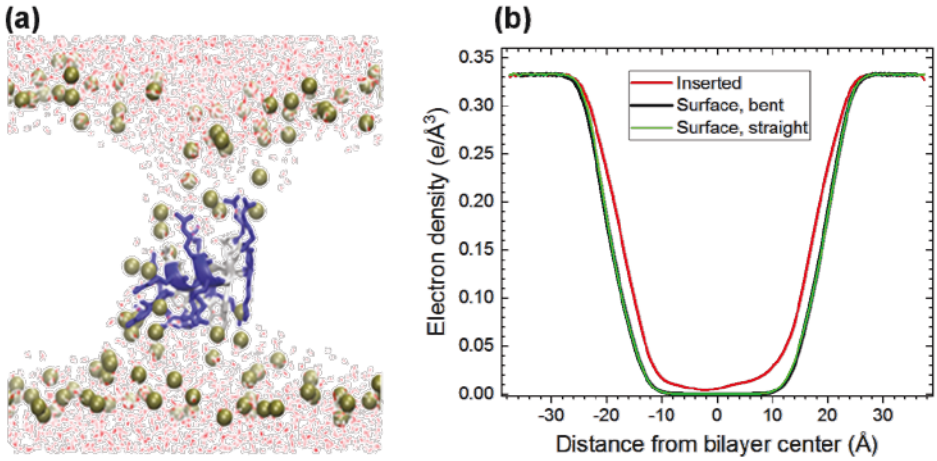

Figure 7. (a) VMD visualization of WLBU2 inserted into G(-) membrane. Colors: WLBU2, ribbon + licorice (R, blue; V,W, grey; K^+ ions, yellow spheres; water, red sticks). (b) Water electron density of G(-) bilayer with WLBU2 either inserted (red line), or on the surface in two different conformations (green and black lines (superimposed)).

The MD simulation gives information about the location of the three types of amino acids across the bilayer. In order to see these visually, we have plotted the groupings of R, W and V in

Fig. 8. These amino acid locations were obtained directly from the MD simulation, using the SimtoExp program, which calculates density in 0.5 Å slices through the bilayer thickness[25, 32]. For the two surface models, R is closest to the aqueous phase, followed by V and then W, which is closest to the interface between headgroups and hydrocarbon chains (near the carbonyl-glycerol group). These locations of amino acids follow their hydrophobicity, with W the most hydrophobic[33]. For the inserted model, R stretches the length of the hydrocarbon core and into the glycerol-carbonyl region, while W is located near the interfacial region and V deep into the hydrocarbon region. Therefore, in the inserted model, the amino acid residues do not follow their hydrophobicities. In Fig. 8 the phosphate + outer headgroup and glycerol-carbonyl components from Fig. 6(e) are superimposed on the amino acid density in order to visualize their relative locations.

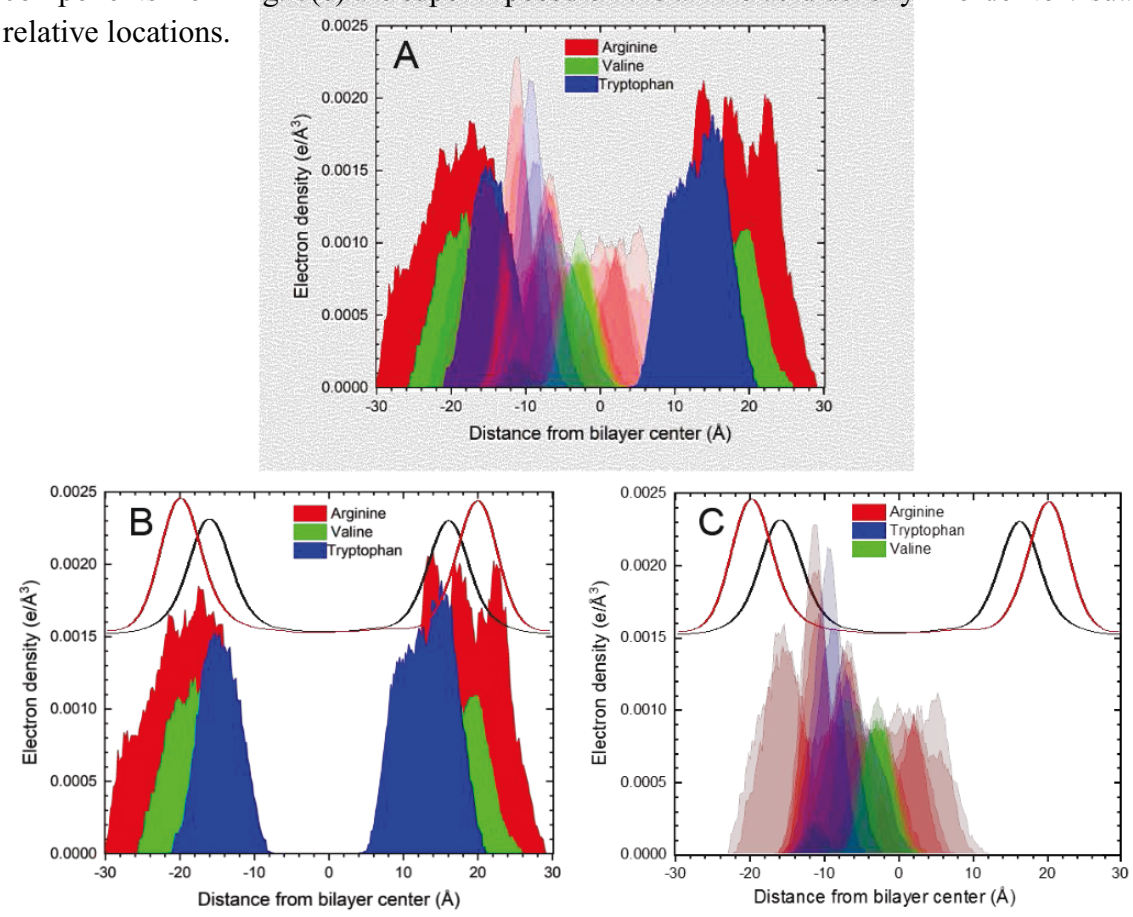

Figure 8. (a) The molecular locations relative to the bilayer center of the three types of amino acids in WLBU2 in G(-) membrane mimic. While Fig. 8(a) shows surface and inserted models superimposed, Fig. 8(b) shows the two surface models, and Fig. 8(c) shows the inserted model. Results are for the non-symmetrized simulation. Colors: R, red; W, blue; V, green. The positions of the phosphate + outer headgroup (red line) and glycerol-carbonyl (black line) are superimposed (lines not drawn to scale) on the amino acid electron density (to scale).

G(+) Membrane

For G(+) LMM, good agreement occurred between simulated and experimental form factors for the control without an applied surface tension. When the peptide WLBU2 was added to the G(+) membrane mimic, the best agreement with experiment was obtained when the peptide simulated density was split into both a bent surface model at 9 dyne/cm and a bent inserted model at 15 dyne/cm. The goodness of fit was not affected by the presence of Na^+ ions, since their amount is ~10X smaller than in the KDO2 simulation. Weighting of the surface and inserted models was constrained to 54% surface and 46% inserted based on integrating the intensity under the peaks in the NR result (Fig. S4(c)). The results shown in Fig. 9 represent the best fit of the experimental data to variations in peptide conformation, surface tension and peptide location. The straight, surface conformation results are not shown since the agreement with experiment was worse, as determined by the chi-square fitting in the SimtoExp program. Note that in Fig. 9(g), significant oxygens on the glycerol/carbonyl, phosphate and water groups (red spheres) enter into the hydrocarbon region when WLBU2 is inserted near the center of the bilayer. Water and Na^+ ions (not shown) are transported through the bilayer due to the internal location of WLBU2.

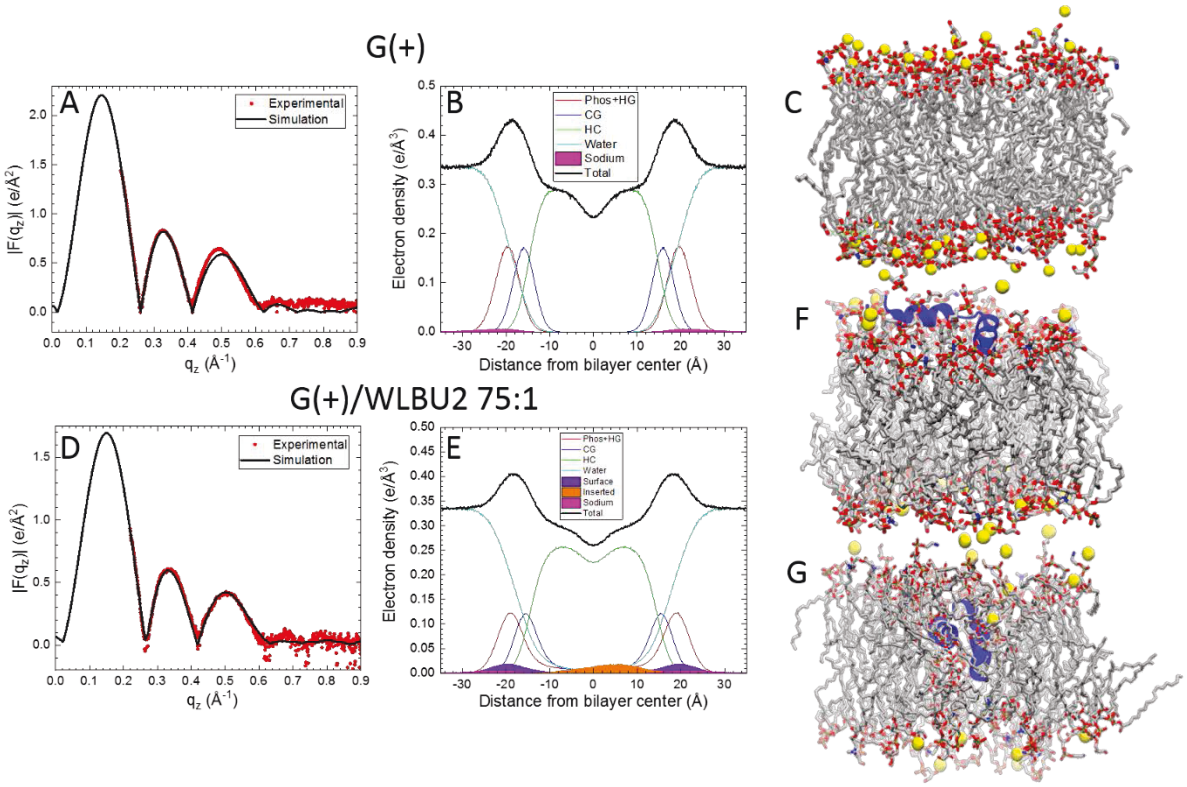

Figure 9. (a) Form factors of experimental (red circles) and simulated G(+) control (black line) at 0 dyne/cm surface tension. (b) Electron density profile of control G(+), colors in legend. (c) VMD visualization of G(+) control. Colors: carbon, gray sticks; oxygen, red spheres. (d) Form factors of experimental data (red circles) with the combined simulated form factors G(+)/WLBU2 80:1 (black lines). (e) Combined simulated electron density profiles G(+)/WLBU2 80:1, colors in legend. Combined signifies 54% WLBU2 in a headgroup location at 9 dyne/cm plus 46% WLBU2 in a hydrocarbon location at 15 dyne/cm. (f) VMD visualization of G(+)/WLBU2 80:1 (bent, surface conformation at 9 dyne/cm). (g) VMD visualization of G(+)/WLBU2 80:1 (bent, inserted conformation at 15 dyne/cm). Colors for F and G as in C, with WLBU2 as a blue ribbon. G(+) LMM: POPG:POPE:DOTAP:TOCL (6:1.5:1.5:1 molar ratio).

The molecular locations of the three classes of amino acids in WLBU2 in the G(+) membrane mimic are shown in Fig. 10(a), with the surface amino acids opaque, and the inserted amino acids semi-transparent. For the surface model in this symmetrized membrane, R and V are closest to the aqueous phase, while W is more deeply buried, as expected from its greater hydrophobicity[33]. For inserted WLBU2, W's lodge closer to the interface than does V, while R spans the entire hydrophobic width. These amino acid locations are similar to the G(-) IM LMM. When the water electron density is plotted (Fig. 10(b)), it shows that significant water enters into the bilayer in the combined model of WLBU2 in the headgroup (54%) and in the hydrocarbon locations (46%) compared to the control.

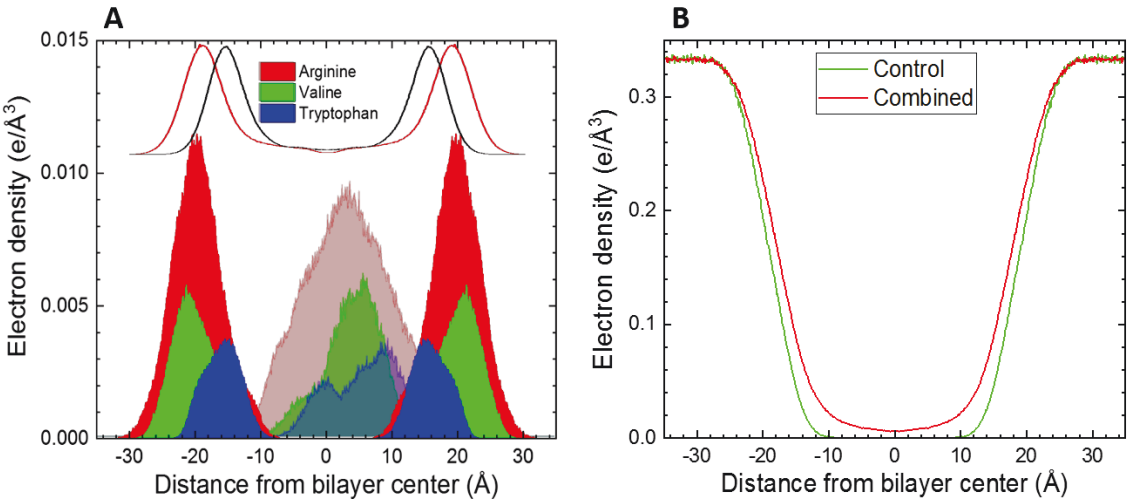

Figure 10. (a) Locations of all of the amino acids in WLBU2 in the bent surface and bent inserted models in the G(+) LMM. Colors in legend. Surface model is opaque, inserted model is transparent. Results are for the symmetrized simulation**.** (b) Water electron density profile in control G(+) and in the combined model (54% HG, 46% HC) of WLBU2 in G(+) LMM. The positions of the phosphate + outer headgroup (red line) and glycerol-carbonyl (black line) are superimposed (lines not drawn to scale) on the amino acid electron density (to scale).

Lipopolysaccharide (LPS)

NR indicated in Fig. 2(d) that WLBU2 is located only in the hydrocarbon region. Therefore, WLBU2 was stabilized in the center of the bilayer. As shown in Fig. 10(a), the agreement is not as good between experimental and simulated form factors as for the other LMMs, even for the control. Several simulations were attempted but were not more successful than in Fig. 11(a). Although our wide-angle x-ray scattering revealed that LPS purified from PA01 is in the fluid phase at 37 $^{\circ}$C since it lacks the sharp chain-chain correlation typical of gel phases (data not shown), this sample did not produce any diffuse x-ray scattering, even at full hydration. Therefore, we included a lipid with LPS that does fluctuate (DLPG) in order to obtain diffuse scattering. When the simulation was carried out with the same mixture of LPS and DLPG as in our experiment (9:1 molar ratio), no better agreement was obtained than when pure LPS was simulated. Simulated results shown in Fig. 10, therefore, are for pure LPS. When the simulated Na^+ ions were included in this comparison, the agreement was worse as judged by the chi-square in the SimtoExp program and so they were not included for the same reasons as with KDO2. In Fig. 11(a) and 11(d), good agreement between experimental and simulated form factors is obtained only in the q_z region between 0.2 and 0.3 $Å^{-1}$. For the rest of these noisy experimental data, the zeroes, or cross-over points, are not clearly defined. However, this flattened-out form factor is clearly different from form factors for KDO2 (Fig. S1(a) and S1(d)), suggesting that the bulky core sugar residues beyond the two octulosonic acid residues are the reason for the degradation of the x-ray form factors.

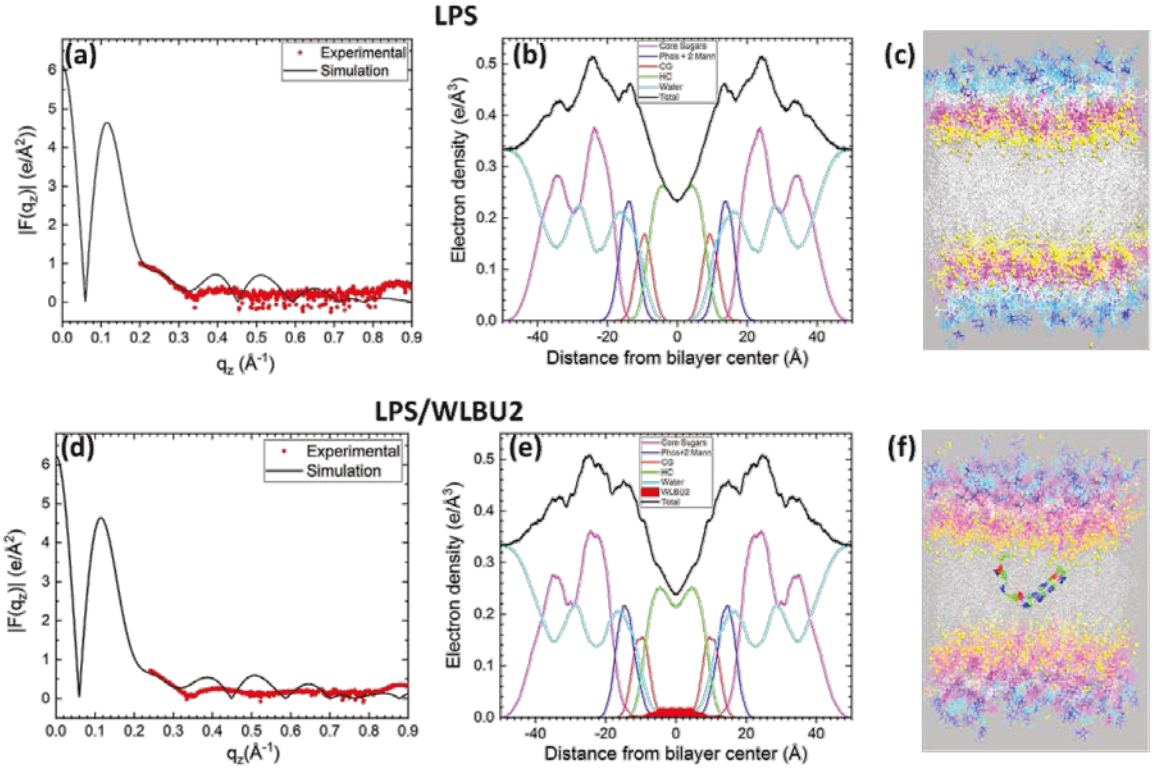

Figure 11. (a) LPS simulated (black line) and experimental form factors (red circles). (b) LPS simulated EDP. Colors: Total, black; core sugars, magenta; phosphate + two mannose residues, blue; carbonyl-glycerol, red; hydrocarbon, green; water, cyan. (c) VMD visualization of LPS control. Colors: Na^+ ions, yellow; two mannose residues, magenta; phosphate groups, white; core sugars, cyan and blue; hydrocarbon chains, light gray. (d) LPS + WLBU2, 75:1, simulated (black line) and experimental form factors (red circles). (e) LPS:WLBU2 75:1 simulated EDP. (f) VMD visualization of LPS:WLBU2 75:1. Colors: as in 10(c). Colors in WLBU2: R, green; V, blue; W, red. Results are for the symmetrized simulation.

Fig. 12 shows that significant water enters into the thin, hydrocarbon core when WLBU2 is inserted into the LPS membrane. Table 2 summarizes the structural results obtained from the simulations for the four LMMs with and without WLBU2.

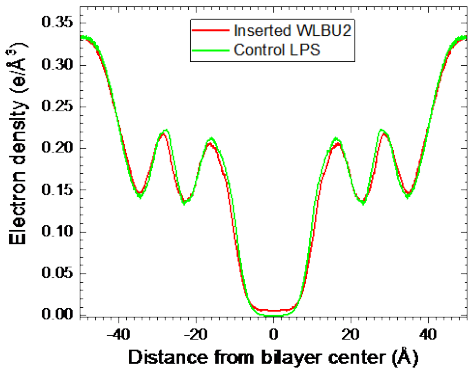

Figure 12. Electron density of water in control LPS (green) and in LPS:WLBU2 75:1 (red).

Table 2. Summary of structural results

Lipid system	**Surface Tension**	**Area (Å^2)**	**2D$_C$ (Å)**
KDO2 control (-6 e)	0 dyne/cm	160.3 ± 0.9	25.4 ± 0.2
[*KDO2 control (-4 e)*]	0 dyne/cm	172.8 ± 2.3	24.0 ± 0.2
KDO2/WLBU2 (-4 e)	0 dyne/cm	171.3 ± 2.0	24.5 ± 0.2
G(-) control	9 dyne/cm	70.4 ± 1.2	29.6 ± 0.2
G(-)/WLBU2*	11 dyne/cm	74.9 ± 0.2	29.0 ± 0.2
G(+) control	0 dyne/cm	70.2 ± 1.7	29.0 ± 0.2
G(+)/WLBU2**	12 dyne/cm	80.9 ± 2.8	28.1 ± 0.2
[*LPS (-10 e)*]	0 dyne/cm	176.7 ± 1.0	18.6 ± 0.2
LPS (-8 e)	0 dyne/cm	179.6 ± 0.6	18.0 ± 0.2
LPS/WLBU2 (-8 e)	0 dyne/cm	178.9 ± 1.1	18.2 ± 0.2

*87.4 G(-) lipids:1 WLBU2, combined surface tension 11.2 dyne/cm.
**combined 11.8 dyne/cm
Simulated samples italicized in brackets [] had a poorer agreement with experimental data determined as determined by the chi-square in the SimtoExp program. Areas were calculated from the final 100 ns of the simulation as described in Materials and Methods. Hydrocarbon bilayer thicknesses (2D$_C$) were estimated from the Gibbs dividing surface of the lipid chain region in the EDP from the simulation.

Discussion

While MD simulation is a powerful tool to visualize molecules and measure molecular distances, equilibration of unbiased simulations to reach an equilibrated state of peptides in the membrane can require >0.8 μs[34]. One way to circumvent this problem is to carry out coarse grain simulations on millisecond time scales[34]. Then, back-transforming (back-mapping) from coarse grain to atomistic simulation can be performed in order to visualize the atomistic configurations of the lipid and peptide molecules[35]. This multiscale approach is valuable and has yielded many innovative publications[36-42]. Another method to shorten the atomistic simulation time of adding peptides to membranes is to allow the peptide and lipids to self-assemble together into a lipid bilayer with peptide incorporated[43]. Another method is a steered molecular dynamics simulation whereby a peptide is pulled into the membrane and allowed to equilibrate[44]. An alternative approach is to compare biased all-atom peptide simulations with peptide-membrane placement to some form of fully equilibrated experimental data. Studies have compared atomistic simulation to small-angle x-ray scattering (SAXS)[45], atomic force microscopy (AFM) [46], nuclear magnetic resonance (NMR)[47], circular dichroism (CD) and NMR[48], analytical ultracentrifugation and ^{13}C NMR[49], sum frequency generation (SFG) vibrational spectroscopy and ATR-FTIR[50], fluorescence microscopy[51] and CD spectroscopy[52]. These experimental techniques can validate the percentage helical content in the peptide (CD and NMR), the amount of aggregation (analytical ultracentrifugation and ^{13}C NMR), the orientation of a peptide in a membrane (SFG and ATR-FTIR), or multimer formation (SAXS and AFM). In the present work we used equilibrium x-ray diffuse scattering (XDS) to determine the lipid bilayer thickness. The MD simulations were constrained to this thickness if necessary by placing a surface tension in the simulation box until the experimental and simulated form factors agreed. In addition, neutron reflectivity (NR) provided the location of the peptide in the membrane, which was the starting point for the atomistic simulations. Thus, biased equilibrium simulations to peptide placement and lateral lipid packing can decrease the required atomistic simulation time and also provide insights into peptide orientation.

A recent similar investigation using MD simulation and NMR spectroscopy indicates that the area/lipid increases from KDO2 (Re LPS mutant) to LPS containing six core sugar residues (Rc LPS mutant)[24], which is in agreement with our increase in area/lipid from Re to LPS containing 10 core sugar residues (Ra LPS mutant) (Table 2). Similarly, both investigations observe a decrease in bilayer thickness from KDO2 to LPS, although the hydrophobic bilayer thickness reported in this work for LPS Ra mutant is 6 Angstroms smaller than that for the Rc mutant (Fig. 5 in [24]). This difference could be related to the increased fluctuations caused by additional sugar residues, thus fluidizing the membrane [53]. Alternatively it could be because Rice et al. used *Salmonella enterica* LPS, whereas we used *Pseudomonas aeruginosa01* LPS. For the counterion in our MD simulation, KDO2 and LPS were both neutralized with Na^+ ions, while in our experiment KDO2 was neutralized with ammonium ions and *PA01* LPS was neutralized with acid. We previously reported that agreement between the simulated and

experimental KDO2 form factors was excellent when Na^+ ions in the simulation were omitted for the comparison, presumably because the ammonium ions diffuse away from the hydrated membrane and their electron density is not as high as sodium ions'[15]. For the LPS comparison of experiment and simulation we also obtained better agreement if the Na^+ ions were omitted. In Rice et al. there was a 2-3% decrease in area/lipid as the negative charge was reduced for both Re LPS and Rc LPS [24] when Na^+ counterions were used, while in our study, area/lipid increased for both Re LPS and Ra LPS as the negative charge was reduced (Table 2). Another difference between our works is that Rice et al. used Amber, while we found this methodology to result in poor agreement with experiment. Further investigation will be needed to determine the source of these minor discrepancies.

What do our results mean for WLBU2's mechanism of action for killing bacteria? Let us first consider KDO2, where NR and MD simulations locate the peptide in the headgroup region. In Fig. S1(f), the VMD visualization shows WLBU2 with the R residues facing downward on the surface of the KDO2 membrane. A cartoon structure of KDO2 is shown in Fig. 13, depicting the charges on the octulosonic acid residues and phosphates on the mannose residues. In the MD simulation, WLBU2 was placed in the water phase above the membrane, and it then migrated towards the surface of KDO2, where it remained for the duration of the 400 ns simulation, failing to reach the phosphate groups (Fig. S1(e)).

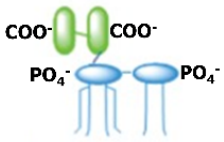

Figure 13. Cartoon structure of KDO2. Colors: octulosonic acid residues, green ellipsoids; mannose residues, blue ellipsoids.

In order for WLBU2 to kill bacteria it must translocate across the outer membrane, through the periplasmic space, and then perturb the inner membrane in G(-) bacteria. Since KDO2 is a rare, rough mutant of LPS, this AMP headgroup location may not be typical for the outer membrane of most G(-) bacteria. We have shown previously that the abundance of carbohydrate residues in the LPS headgroup causes increased membrane fluctuations, which could facilitate peptide entry into the hydrocarbon interior[54]. For LPS, NR in Fig. S4(d) indicates that WLBU2 is located only in the hydrocarbon interior. The VMD visualization of WLBU2 in LPS in Fig. 10(f) shows the bent conformation, with ~50% α-helix, which is similar to the ~40% α-helix determined by CD[15]. This interior location would facilitate self-promoted uptake[55] of WLBU2 through the outer membrane that must occur in order for it to reach the inner membrane. When the highly positively charged arginine residues embed deep into the hydrocarbon phase, they cause water to enter. This is shown in Fig. 12, where there is significant electron density of water at the center of the bilayer with embedded WLBU2 in LPS. Therefore, in the first step of bacterial killing as WLBU2 encounters the negatively charged bacterial membrane, we suggest it binds to the carboxyl groups on the octulosonic acid residues,

and then penetrates into the hydrocarbon interior with accompanying water due to the considerable membrane fluctuations.

Traditionally, the outer membrane (OM) has been thought of as the major permeability barrier to antibiotics. Conventional antibiotics such as beta-lactams, are thought to enter the OM through pores formed by porin proteins[56], but generally, only hydrophilic substances less than 600 Daltons can diffuse through the porins. In addition, the OM has an unusually low permeability to hydrophobic molecules[57], while cationic AMPs, like WLBU2, are able to permeate the membrane similarly to cell-penetrating peptides due to their interaction with negatively charged lipid headgroups[58]. The simulation visualization in Fig. 11(f) shows that two of the R's are closer to the interfacial region, while V and W are equally present at all depths in the hydrocarbon region, which suggests that the bent configuration is correct. The location of R closer to the interface may be important in drawing water into the membrane.

Presumably WLBU2 then exits the outer membrane and enters the periplasmic space. The periplasm has many functions, including protein secretion and folding, environmental sensing, peptidoglycan synthesis, osmoregulation, resistance to turgor pressure, and sensing and resistance to cationic antimicrobial peptides[59]. Within the periplasmic space is a layer of crosslinked sugars and amino acids termed peptidoglycan, which is linked to the outer membrane through covalent linkages to the outer membrane lipoprotein. Multicomponent protein complexes such as the flagellar machine span the two membranes. Due to its constituents, the periplasmic space is osmotically active. A Donnan equilibrium controls the flow of water and ions from the cytoplasm, or from the extracellular fluid, to the periplasm[58] and it is generally thought that the gel-like periplasm is fairly permeable to small molecules like antibiotics and AMPs[58].

For G(-) bacteria the AMPs next encounter the inner membrane (IM). Our NR results revealed in Fig. S5(b) that WLBU2 finds two locations in the IM: 63% in the headgroup and 37% in the hydrocarbon interior. This dual location may be important for WLBU2's function of perturbing the membrane and killing the bacteria. In the surface states, Fig. 8 shows that R spans the range from 12 to 30 Å, V spans 14 to 26 Å and W spans 8 to 21 Å from the bilayer center. The outermost position for R is consistent with its smallest hydrophobicity[33]. R extends to the bulk water phase and is in position to bind to the phosphate headgroup of G(-) LMM near 20 Å from the bilayer center (see Fig. 8(b)). In the inserted state, R spans a region from the headgroup in the proximal monolayer to the hydrocarbon edge in the distal monolayer. Thus, even when R is in the hydrocarbon region, it has a portion that can bind to the phosphate headgroup. This electrostatic binding must be crucial in anchoring WLBU2 to the lipid headgroup region in the G(-) inner membrane, while still penetrating deep into the hydrocarbon region. W has a component at the bilayer interfacial region at 14 Å when in both the surface and inserted states, which is a second anchor that keeps WLBU2 from fully penetrating the hydrocarbon interior.

G(+) membrane/WLBU2 interaction is similar to that of G(-) membrane, which is reasonable since WLBU2 kills both types of bacteria efficiently[15]. Our NR results revealed in Fig. S5(c) that WLBU2 finds two locations in G(+): 54% in the headgroup and 46% in the hydrocarbon interior. One difference compared to G(-) membrane is that the headgroup and hydrocarbon positions of WLBU2 are better separated in G(+) than in G(-) IM (compare Fig. 10(a) to Fig. 8(a)), but R in the bent surface state in G(+) is again aligned at the phosphate position near 20 Å from the bilayer center. W is again aligned with the interfacial region at ~ 15 Å from the bilayer center. When WLBU2 is in the bilayer interior, R overlaps with the surface R state, thus forming a continuous positive charge across the bilayer, while W and V are centrally located. The continuous line of positive charges allows water to enter the hydrocarbon interior creating a pathway for water and ions to leave the bacterial cell, thereby killing it.

In this work we have not explored the question of AMP aggregation and how aggregated WLBU2s might interact with the membrane. A role for aggregation in selectivity between a eukaryotic and bacterial membrane model was investigated for the fungicide fengycin[60] at a much higher lipid:peptide molar ratio than in this work, since we constrained our peptide concentration to the highest permissible in the XDS experiment (76:1). In addition, fengycin contains a lipophilic tail which could cause aggregation via van der Waals attractive interactions. Similarly in a study of the AMP polymyxin E (colistin) on planar lipid bilayers composed of LPS/PC, it was found that colistin, which also contains a lipophilic tail, induces large-scale clustering as it segregates out LPS[61]. Since WLBU2 is highly positively charged (+13), it is unlikely that self-aggregation would occur, even when binding to phosphate headgroups.

To summarize, this work reports on the use of neutron and x-ray diffuse scattering to shorten the time required for AA MD simulations. By constraining the thickness of the simulated membrane using a surface tension to match that obtained by XDS experiments, and by constraining the location of the peptide in the membrane to match that obtained by neutron reflectometry, microsecond simulations are not required. Importantly, constraints on peptide location are finally removed, allowing equilibration. One important molecular result in this investigation is the observation of water at the center of the bilayer when WLBU2 is in the inserted state. Other investigations of the KvAP voltage-gated potassium channel[44, 62] and the HIV Tat protein[63] have also found water with charged amino acid residues that are buried in the hydrocarbon interior. In the case of WLBU2, the internal water is continuous with the headgroup water due to a dual anchoring of WLBU2 in the headgroup and in the interfacial region, and also penetration into the hydrocarbon region. Arginine's binding to phosphate residues, plus tryptophan's location near the bilayer interface may be important anchoring mechanisms in the membrane perturbations. WLBU2 causes a small (~1 Å) thinning at a lipid:peptide molar ratio of ~76:1 in all four LMMs. An increase in area per lipid (APL) with the addition of WLBU2 is observed in every case except for LPS, where a small decrease in APL is observed. Thus, the dual location of WLBU2 in the headgroup and hydrocarbon regions, the presence of water in the interior and the location of arginines at the phosphate and tryptophans at

the interfacial region, the slight bilayer thinning all contribute to membrane destabilization thus killing bacteria.

Supporting Information

S.I. contains Materials and Methods and Results for KDO2 simulations, MD stability tests, NR and XDS in Figs. S1-S6.

Author Contributions

Robert Allsopp, Anna Pavlova, Tyler Cline: Software, Visualization, Formal analysis, Methodology
Jeffery Klauda, James Gumbart: Data curation, Funding acquisition, Resources, Supervision
Aria Salyapongse: Formal analysis
Richard Gillilan: Investigation
Y. Peter Di, Berthony Deslouches: Writing, review and editing
Stephanie Tristram-Nagle: Conceptualization, Validation, Investigation, Formal analysis, Data curation, Writing – original draft, Supervision, Project Administration, Funding acquisition

Declaration of Interests: The authors declare no competing interests.

Accession Numbers

The structures in this work were deposited in the Small Angle Scattering Biological Data Bank (SASBDB) on January 17, 2022. Their #'s are: **SASDNU4, SASDNV4, SASDNW4, SASDNX4, SASDNY4, SASDNZ4, SASDN25** and **SASDN35.** They will "go live" upon publication of this paper.

Acknowledgments

This work is based upon research conducted at Carnegie Mellon University and at the Center for High Energy X-ray Sciences (CHEXS), which is supported by the National Science Foundation under award DMR-1829070, and the Macromolecular Diffraction at the Cornell High Energy Synchortron Sources (CHESS) (MacCHESS) facility, which is supported by award 1-P30-GM124166-01A1 from the National Institute of General Medical Sciences, National Institutes of Health, and by New York State's Empire State Development Corporation (NYSTAR). The authors would like to thank Drs. Irina Kriksunov and Qingqiu Huang for help with the virtual data collection at CHESS beamline ID7A1. Additional support for this work was from Carnegie Mellon SURF (A.S.), National Institutes of Health (NIH) R01AI133351 (Y.P.D., S.T.N.), NIH R01GM125917 (B.D., S.T.N.), NIH R01GM123169 (J.C.G., A.P.), National Science Foundation (NSF) MCB-2115790 (S.T.N.) and NSF MCB-1951425 (J.K., R.A.). Simulations were performed on the Extreme Science and Engineering Discovery Environment (XSEDE) supercomputers, which are supported by NSF grant ACI-1548562, under allocations MCB-100139 and MCB-130183, and on Comet and Expanse at the San Diego Super-computer Center at U.C. San Diego.

References

1. WHO, Antimicrobial resistance WHO global report on surveillance. *http://www.who.int/drugresistance/documents/surveillancereport/en/* **2014**.
2. O'Niell, J. *Tackling drug-resistant infections globally: Final report and recommendations*; United Kingdom, 2016; pp 1-84.
3. Durr, U. H. N.; Sudheendra, U. S.; Ramamoorthy, A., LL-37, the only human member of the cathelicidin family of antimicrobial peptides. *Bba-Biomembranes* **2006,** *1758* (9), 1408-1425.
4. Deslouches, B.; Islam, K.; Craigo, J. K.; Paranjape, S. M.; Montelaro, R. C.; Mietzner, T. A., Activity of the de novo engineered antimicrobial peptide WLBU2 against Pseudomonas aeruginosa in human serum and whole blood: implications for systemic applications. *Antimicrob Agents Chemother* **2005,** *49* (8), 3208-3216.
5. Tencza, S. B.; Creighton, D. J.; Yuan, T.; Vogel, H. J.; Montelaro, R. C.; Mietzner, T. A., Lentivirus-derived antimicrobial peptides: increased potency by sequence engineering and dimerization. *The Journal of antimicrobial chemotherapy* **1999,** *44* (1), 33-41.
6. Lohner, K., The role of membrane lipid composition in cell targeting of antimicrobial peptides. In *Development of Novel Antimicrobial Agents: Emerging Strategies*, Lohner, K., Ed. Horizon Scientific Press: 2001; pp 149-165.
7. Deslouches, B.; Gonzalez, I. A.; DeAlmeida, D.; Islam, K.; Steele, C.; Montelaro, R. C.; Mietzner, T. A., De novo-derived cationic antimicrobial peptide activity in a murine model of Pseudomonas aeruginosa bacteraemia. *The Journal of antimicrobial chemotherapy* **2007,** *60* (3), 669-672.
8. Chen, C.; Deslouches, B.; Montelaro, R. C.; Di, Y. P., Enhanced efficacy of the engineered antimicrobial peptide WLBU2 via direct airway delivery in a murine model of Pseudomonas aeruginosa pneumonia. *Clin Microbiol Infec* **2018,** *24* (5), 547(e1-e8).
9. Deslouches, B.; Steckbeck, J. D.; Craigo, J. K.; Doi, Y.; Mietzner, T. A.; Montelaro, R. C., Rational design of engineered cationic antimicrobial peptides consisting exclusively of arginine and tryptophan, and their activity against multidrug-resistant pathogens. *Antimicrob Agents Chemother* **2013,** *57* (6), 2511-2521.
10. Steckbeck, J. D.; Deslouches, B.; Montelaro, R. C., Antimicrobial peptides: new drugs for bad bugs? *Expert opinion on biological therapy* **2014,** *14* (1), 11-4.
11. Lashua, L. P.; Melvin, J. A.; Deslouches, B.; Pilewski, J. M.; Montelaro, R. C.; Bomberger, J. M., Engineered cationic antimicrobial peptide (eCAP) prevents Pseudomonas aeruginosa biofilm growth on airway epithelial cells. *J Antimicrob Chemoth* **2016,** *71* (8), 2200-2207.
12. Deslouches, B.; Steckbeck, J. D.; Craigo, J. K.; Doi, Y.; Burns, J. L.; Montelaro, R. C., Engineered cationic antimicrobial peptides to overcome multidrug resistance by ESKAPE pathogens. *Antimicrob Agents Chemother* **2015,** *59* (2), 1329-1333.
13. Deslouches, B.; Phadke, S. M.; Lazarevic, V.; Cascio, M.; Islam, K.; Montelaro, R. C.; Mietzner, T. A., De novo generation of cationic antimicrobial peptides: influence of length and tryptophan substitution on antimicrobial activity. *Antimicrob Agents Chemother* **2005,** *49* (1), 316-322.
14. Huang, D., Dobbins, D., Ghahramani, P., Friedland, I., Steckbeck, J., A phase 1 study of safety, tolerability and pharmacokinetics of single ascending doses of a first in human engineered cationic peptides, PLG0206, intravenously administered in healthy subjects. *Antimicrob Agents Chemother* **2021**, [Preprint], doi: https://doi.org/10.1128/AAC.01441-21.
15. Heinrich, F.; Salyapongse, A.; Kumagai, A.; Dupuy, F. G.; Shukla, K.; Penk, A.; Huster, D.; Ernst, R. K.; Pavlova, A.; Gumbart, J. C.; Deslouches, B.; Di, Y. P.; Tristram-Nagle, S., Synergistic biophysical techniques reveal structural mechanisms of engineered cationic antimicrobial peptides in lipid model membranes. *Chemistry - A European Journal* **2020,** *26*, 6247 – 6256.

16. Ratledge, C.; Wilkinson, S. G., *Microbial lipids*. Academic Press: London ; San Diego, 1988.
17. Durell, S. R.; Brooks, B. R.; Bennaim, A., Solvent-induced forces between two hydrophilic groups. *J Phys Chem-Us* **1994,** *98* (8), 2198-2202.
18. Phillips, J. C.; Hardy, D. J.; Maia, J. D. C.; Stone, J. E.; Ribeiro, J. V.; Bernardi, R. C.; Buch, R.; Fiorin, G.; Henin, J.; Jiang, W.; McGreevy, R.; Melo, M. C. R.; Radak, B. K.; Skeel, R. D.; Singharoy, A.; Wang, Y.; Roux, B.; Aksimentiev, A.; Luthey-Schulten, Z.; Kale, L. V.; Schulten, K.; Chipot, C.; Tajkhorshid, E., Scalable molecular dynamics on CPU and GPU architectures with NAMD. *J Chem Phys* **2020,** *153* (4), 044130.
19. Klauda, J. B.; Venable, R. M.; Freites, J. A.; O'Connor, J. W.; Tobias, D. J.; Mondragon-Ramirez, C.; Vorobyov, I.; MacKerell, A. D.; Pastor, R. W., Update of the CHARMM all-atom additive force field for lipids: Validation on six lipid types. *Journal of Physical Chemistry B* **2010,** *114* (23), 7830-7843.
20. Huang, J.; Rauscher, S.; Nawrocki, G.; Ran, T.; Feig, M.; de Groot, B. L.; Grubmuller, H.; MacKerell, A. D., CHARMM36m: an improved force field for folded and intrinsically disordered proteins. *Nat Methods* **2017,** *14* (1), 71-73.
21. Darden, T.; York, D.; Pedersen, L., Particle mesh Ewald - an N.log(N) method for Ewald sums in large systems. *J Chem Phys* **1993,** *98* (12), 10089-10092.
22. Jo, S.; Kim, T.; Iyer, V. G.; Im, W., CHARMM-GUI: a web-based graphical user interface for CHARMM. *Journal of computational chemistry* **2008,** *29* (11), 1859-65.
23. Wu, E. L.; Cheng, X.; Jo, S.; Rui, H.; Song, K. C.; Davila-Contreras, E. M.; Qi, Y. F.; Lee, J. M.; Monje-Galvan, V.; Venable, R. M.; Klauda, J. B.; Im, W., CHARMM-GUI membrane builder toward realistic biological membrane simulations. *Journal of computational chemistry* **2014,** *35* (27), 1997-2004.
24. Rice, A.; Rooney, M. T.; Greenwood, A. I.; Cotten, M. L.; Wereszczynski, J., Lipopolysaccharide simulations are sensitive to phosphate charge and ion parameterization. *J Chem Theory Comput* **2020,** *16* (3), 1806-1815.
25. Kucerka, N.; Katsaras, J.; Nagle, J. F., Comparing membrane simulations to scattering experiments: Introducing the SIMtoEXP software. *J Membrane Biol* **2010,** *235* (1), 43-50.
26. Raman, S.; Vernon, R.; Thompson, J.; Tyka, M.; Sadreyev, R.; Pei, J. M.; Kim, D.; Kellogg, E.; DiMaio, F.; Lange, O.; Kinch, L.; Sheffler, W.; Kim, B. H.; Das, R.; Grishin, N. V.; Baker, D., Structure prediction for CASP8 with all-atom refinement using Rosetta. *Proteins* **2009,** *77*, 89-99.
27. Song, Y. F.; DiMaio, F.; Wang, R. Y. R.; Kim, D.; Miles, C.; Brunette, T. J.; Thompson, J.; Baker, D., High-resolution comparative modeling with RosettaCM. *Structure* **2013,** *21* (10), 1735-1742.
28. Humphrey, W.; Dalke, A.; Schulten, K., VMD: Visual molecular dynamics. *J Mol Graph Model* **1996,** *14* (1), 33-38.
29. Jo, S.; Cheng, X.; Lee, J.; Kim, S.; Park, S. J.; Patel, D. S.; Beaven, A. H.; Lee, K. I.; Rui, H.; Park, S.; Lee, H. S.; Roux, B.; MacKerell, A. D.; Klauda, J. B.; Qi, Y. F.; Im, W., CHARMM-GUI 10 years for biomolecular modeling and simulation. *Journal of computational chemistry* **2017,** *38* (15), 1114-1124.
30. Lee, J.; Patel, D. S.; Stahle, J.; Park, S. J.; Kern, N. R.; Kim, S.; Lee, J.; Cheng, X.; Valvano, M. A.; Holst, O.; Knirel, Y. A.; Qi, Y. F.; Jo, S.; Klauda, J. B.; Widmalm, G.; Im, W., CHARMM-GUI membrane builder for complex biological membrane simulations with glycolipids and lipoglycans. *J Chem Theory Comput* **2019,** *15* (1), 775-786.
31. Loney, R. W.; Panzuela, S.; Chen, J.; Yang, Z. M.; Fritz, J. R.; Dell, Z.; Corradi, V.; Kumar, K.; Tieleman, D. P.; Hall, S. B.; Tristram-Nagle, S. A., Location of the hydrophobic surfactant proteins, SP-B and SP-C, in fluid-phase bilayers. *Journal of Physical Chemistry B* **2020,** *124* (31), 6763-6774.
32. Petrache, H. I.; Feller, S. E.; Nagle, J. F., Determination of component volumes of lipid bilayers from simulations. *Biophysical journal* **1997,** *72* (5), 2237-2242.
33. Wimley, W. C.; White, S. H., Experimentally determined hydrophobicity scale for proteins at membrane interfaces. *Nat Struct Biol* **1996,** *3* (10), 842-848.

34. Deserno, M., Mesoscopic membrane physics: concepts, simulations, and selected applications. *Macromol Rapid Comm* **2009,** *30* (9-10), 752-771.
35. Wassenaar, T. A.; Pluhackova, K.; Bockmann, R. A.; Marrink, S. J.; Tieleman, D. P., Going backward: A flexible geometric approach to reverse transformation from coarse grained to atomistic models. *J Chem Theory Comput* **2014,** *10* (2), 676-690.
36. Monticelli, L.; Kandasamy, S. K.; Periole, X.; Larson, R. G.; Tieleman, D. P.; Marrink, S. J., The MARTINI Coarse-Grained Force Field: Extension to Proteins. *J Chem Theory Comput* **2008,** *4* (5), 819-34.
37. Rzepiela, A. J.; Schafer, L. V.; Goga, N.; Risselada, H. J.; De Vries, A. H.; Marrink, S. J., Reconstruction of atomistic details from coarse-grained structures. *Journal of computational chemistry* **2010,** *31* (6), 1333-1343.
38. Rzepiela, A. J.; Sengupta, D.; Goga, N.; Marrink, S. J., Membrane poration by antimicrobial peptides combining atomistic and coarse-grained descriptions. *Faraday Discuss* **2010,** *144*, 431-43; discussion 445-81.
39. Lyubartsev, A. P., Multiscale modeling of lipids and lipid bilayers. *Eur Biophys J Biophy* **2005,** *35* (1), 53-61.
40. Marrink, S. J.; Tieleman, D. P., Perspective on the Martini model. *Chem Soc Rev* **2013,** *42* (16), 6801-6822.
41. Wang, Z. J.; Deserno, M., A Systematically Coarse-Grained Solvent-Free Model for Quantitative Phospholipid Bilayer Simulations. *Journal of Physical Chemistry B* **2010,** *114* (34), 11207-11220.
42. Pluhackova, K.; Bockmann, R. A., Biomembranes in atomistic and coarse-grained simulations. *J Phys-Condens Mat* **2015,** *27* (32).
43. Esteban-Martin, S.; Salgado, J., Self-assembling of peptide/membrane complexes by atomistic molecular dynamics simulations. *Biophysical journal* **2007,** *92* (3), 903-912.
44. Monticelli, L.; Robertson, K. M.; MacCallum, J. L.; Tieleman, D. P., Computer simulation of the KvAP voltage-gated potassium channel: steered molecular dynamics of the voltage sensor. *FEBS letters* **2004,** *564* (3), 325-332.
45. Henriques, J.; Cragnell, C.; Skepo, M., Molecular dynamics simulations of intrinsically disordered proteins: Force field evaluation and comparison with experiment. *J Chem Theory Comput* **2015,** *11* (7), 3420-3431.
46. Jang, H.; Connelly, L.; Arce, F. T.; Ramachandran, S.; Kagan, B. L.; Lal, R.; Nussinov, R., Mechanisms for the insertion of toxic, fibril-like beta-amyloid oligomers into the membrane. *J Chem Theory Comput* **2013,** *9* (1), 822-833.
47. Isaksson, J.; Brandsdal, B. O.; Engqvist, M.; Flaten, G. E.; Svendsen, J. S. M.; Stensen, W., A synthetic antimicrobial peptidomimetic (LTX 109): Stereochemical impact on membrane disruption. *J Med Chem* **2011,** *54* (16), 5786-5795.
48. Sforca, M. L.; Oyama, S.; Canduri, F.; Lorenzi, C. C. B.; Pertinhez, T. A.; Konno, K.; Souza, B. M.; Palma, N. S.; Neto, J. R.; Azevedo, W. F.; Spisni, A., How C-terminal carboxyamidation alters the biological activity of peptides from the venom of the eumenine solitary wasp. *Biochemistry* **2004,** *43* (19), 5608-5617.
49. Ho, S. W.; Jung, D.; Calhoun, J. R.; Lear, J. D.; Okon, M.; Scott, W. R. P.; Hancock, R. E. W.; Straus, S. K., Effect of divalent cations on the structure of the antibiotic daptomycin. *Eur Biophys J Biophy* **2008,** *37* (4), 421-433.
50. Ding, B.; Jasensky, J.; Li, Y. X.; Chen, Z., Engineering and characterization of peptides and proteins at surfaces and interfaces: A case study in surface-sensitive vibrational spectroscopy. *Accounts Chem Res* **2016,** *49* (6), 1149-1157.
51. Orioni, B.; Bocchinfuso, G.; Kim, J. Y.; Palleschi, A.; Grande, G.; Bobone, S.; Park, Y.; Kim, J. I.; Hahm, K. S.; Stella, L., Membrane perturbation by the antimicrobial peptide PMAP-23: A fluorescence and molecular dynamics study. *Bba-Biomembranes* **2009,** *1788* (7), 1523-1533.

52. Kaur, K.; Andrew, L. C.; Wishart, D. S.; Vederas, J. C., Dynamic relationships among type IIa bacteriocins: Temperature effects on antimicrobial activity and on structure of the C-terminal amphipathic alpha helix as a receptor-binding region. *Biochemistry* **2004,** *43* (28), 9009-9020.
53. Kumagai, A.; Dupuy, F. G.; Arsov, Z.; Elhady, Y.; Moody, D.; Ernst, R. K.; Deslouches, B.; Montelaro, R. C.; Di, Y. P.; Tristram-Nagle, S., Elastic behavior of model membranes with antimicrobial peptides depends on lipid specificity and D-enantiomers. *Soft Matter* **2019,** *15* (8), 1860-1868.
54. Dupuy, F. G.; Pagano, I.; Andenoro, K.; Peralta, M. F.; Elhady, Y.; Heinrich, F.; Tristram-Nagle, S., Selective interaction of colistin with lipid model membranes. *Biophysical journal* **2018,** *114* (4), 919-928.
55. Hancock, R. E., Alterations in outer membrane permeability. *Annual review of microbiology* **1984,** *38*, 237-264.
56. James, C. E.; Mahendran, K. R.; Molitor, A.; Bolla, J. M.; Bessonov, A. N.; Winterhalter, M.; Page, J. M., How beta-lactam antibiotics enter bacteria: A dialogue with the porins. *PloS one* **2009,** *4* (5), e5453.
57. Nikaido, H., Outer membrane of Salmonella-typhimurium transmembrane diffusion of some hydrophobic substances. *Biochimica et biophysica acta* **1976,** *433* (1), 118-132.
58. Thoren, P. E. G.; Persson, D.; Karlsson, M.; Norden, B., The Antennapedia peptide penetratin translocates across lipid bilayers - the first direct observation. *FEBS letters* **2000,** *482* (3), 265-268.
59. Miller, S. I.; Salama, N. R., The gram-negative bacterial periplasm: Size matters. *Plos Biol* **2018,** *16* (1).
60. Sur, S.; Romo, T. D.; Grossfield, A., Selectivity and mechanism of fengycin, an antimicrobial lipopeptide, from molecular dynamics. *Journal of Physical Chemistry B* **2018,** *122* (8), 2219-2226.
61. Khadka, N. K.; Aryal, C. M.; Pan, J. J., Lipopolysaccharide-dependent membrane permeation and lipid clustering caused by cyclic lipopeptide colistin. *Acs Omega* **2018,** *3* (12), 17828-17834.
62. Freites, J. A.; Tobias, D. J.; von Heijne, G.; White, S. H., Interface connections of a transmembrane voltage sensor. *Proceedings of the National Academy of Sciences of the United States of America* **2005,** *102* (42), 15059-15064.
63. Neale, C.; Huang, K.; Garcia, A. E.; Tristram-Nagle, S., Penetration of HIV-1 Tat47-57 into PC/PE bilayers assessed by MD simulation and X-ray scattering. *Membranes (Basel)* **2015,** *5* (3), 473-494.

Table of Contents Graphic